

PAPER View Article Online



Cite this: DOI: 10.1039/d2cp04882e

Phase transition of individual anatase TiO₂ microcrystals with large percentage of (001) facets: a Raman mapping and SEM study†

Weigang Lu,‡^a Hao Zhu,‡^a Blake Birmingham,^a Nolan Craft,^a Jonathan Hu, oban Kenneth Park*^a and Zhenrong Zhang oban

TiO₂ has been extensively studied in many fields including photocatalysis, electrochemistry, optics, etc. Understanding the mechanism of the anatase-rutile phase transition (ART) process is critical for the design of TiO₂-based high-activity photocatalysts and tuning its properties for other applications. In this work, the ART process using individual anatase micro-particles with a large percentage of (001) facets was monitored and studied. Phase concentration evolution obtained via Raman microscopy was correlated with the morphological evolution observed in scanning electron microscope (SEM) images. The ART of anatase microcrystals is dominated by surface nucleation and growth, but the ART processes of individual anatase particles are distinctive and depend on the various rutile nucleation sites. Two types of transformation pathways are observed. In one type of ART pathway, the rutile phase nucleated at a corner of an anatase microcrystal and grew in one direction along the edge of the crystal firstly followed by propagation over the rest of the microcrystal in the orthogonal direction on the surface and to the bulk of the crystal. The kinetics of the ART follows the first-order model with two distinct rate constants. The fast reaction rate is from the surface nucleation and growth, and the slow rate is from the bulk nucleation and growth. In the other type of ART pathway, multiple rutile nucleation sites formed simultaneously on different edges and corners of the microcrystal. The rutile phase spread over the whole crystal from these nucleation sites with a small contribution of bulk nucleation. Our study on the ART of individual micro-sized crystals bridges the material gap between bulk crystals and nano-sized TiO2 particles. The anatase/rutile co-existing particle will provide a perfect platform to study the synergistic effect between the anatase phase and the rutile phase in their catalytic performances.

Received 19th October 2022, Accepted 26th December 2022

DOI: 10.1039/d2cp04882e

rsc.li/pccp

Introduction

 TiO_2 has been extensively studied because of its interesting chemical and optical properties. Rutile and anatase are the two main polymorphs of TiO_2 that are easy to synthesize. They have been widely employed in areas such as photocatalysis, $^{1-3}$ electrochemistry, 4,5 photovoltaics, $^{6-8}$ microwave absorption, 9,10 *etc.* In photocatalysis, it is generally accepted that anatase displays higher photocatalytic activities than rutile. $^{11-16}$ Many

studies show that anatase/rutile mixed-phase ${\rm TiO_2}$ has higher photoactivity than the single-phase ${\rm TiO_2}^{17-23}$ with the mixed-phased ${\rm TiO_2}$ P25 being regarded as the "golden standard" for photocatalysis. The synergistic effect between anatase and rutile which enhances the separation of photogenerated electrons and holes has been attributed to the high catalytic activities of mixed-phase ${\rm TiO_2}.^{17-21}$ However, the synergistic mechanism is still under debate. Therefore, understanding the phase transformation process of ${\rm TiO_2}$ is critical for achieving the desired crystal phase for its designed applications.

Anatase is the metastable phase whereas rutile is the stable polymorph under ambient conditions. ^{13,24–29} Anatase–rutile phase transition (ART) is complex as it occurs at a wide temperature range between 400° and 1200 °C^{24–26} depending on grain size, impurities, morphology, sample preparation method, heating process, *etc.* ^{4,14,15,30} Both anatase and rutile are tetragonal but have different space groups, $I4_1/amd$ (a = 3.785 Å, c = 9.514 Å) for anatase and $P4_2/mnm$ (a = 4.594 Å, c = 0.2959 Å) for rutile, ^{31,32} respectively. The TiO₆ octahedra in the unit cell of an anatase

^a Department of Physics, Baylor University, Waco, Texas, 76798, USA. E-mail: Zhenrong_zhang@baylor.edu, Kenneth_park@baylor.edu

b Department of Electrical and Computer Engineering, Baylor University, Waco, Texas. 76798. USA

 $[\]dagger$ Electronic supplementary information (ESI) available: Additional SEM images and Raman spectra of the particles, calculation of percentage of (001) facet of anatase microcrystal, rutile TiO_2 morphological Wulff reconstruction, and quantitative estimation of the weight concentration of the anatase/rutile phase. See DOI: https://doi.org/10.1039/d2cp04882e

[‡] Contribute equally.

crystal share four edges with neighboring octahedra, and ${\rm TiO_6}$ octahedra in the unit cell of a rutile crystal share two edges. Therefore, when the ART takes place, ${\rm TiO_2}$ undergoes a reconstructive process that involves the breaking and reforming of bonds and introduces about 8% volume contraction. 13,36

Qualitative and quantitative phase analyses of titania particles have been performed using various techniques. 25,27,28,37-41 X-ray diffraction (XRD) has been used in the determination of the relative quantities of anatase and rutile components during the phase transition process since the 1950s. The relative percentages were calculated via the intensity ratio of the rutile (110) peak to the anatase (101) peak of titania powder. 14,25,38,42-44 However, the spatial resolution of the XRD is limited to tens of micrometers even with micro XRD. Raman spectra have also been employed for qualitative and quantitative phase analysis because of the clear distinction between the anatase phase and the rutile phase 13,27,28,45,46 with a submicron meter spatial resolution. 47-49 Until recently, the understanding of the ART mechanism and kinetics developed from the XRD and Raman studies was based on the ensemble collections of the scattered light from titania powder samples, which represent the collective phase stability and transformation kinetics of nanoparticles. However, transmission electron microscopy (TEM) studies can directly image atomic-level structure changes of individual nanoparticles during titania aggregations^{43,50} and have shown that the ART process starts with rutile nucleation at anatase {112} twin boundaries. 42 Very recently, in situ TEM investigations have shown different pathways of titania polymorphs' phase transition and electron beam irradiation induced titania phase transition from individual nanoparticles.30 Although the ART process and mechanism have been extensively studied, whether the surface nucleation or bulk nucleation dominates the ART is still a question. 23,27,28 The connection between the phase transition kinetics obtained from ensemble studies and the ART process observed at the single-particle level is also missing because of the mismatch of the size of the nanoparticles and the spatial resolution of these microscopy techniques.

Here, micro-sized single crystalline anatase particles with a large percentage of reactive (001) facets⁵¹⁻⁵⁴ were chosen to study the ART process of a single particle. It is an ideal system that overcomes the "size" issue of TiO₂ nanoparticles and bridges the size gap between the bulk crystal and nanoparticles. It provides various well-defined crystal surface facets to correlate the sub-particle structure with the ART process of a particle. We determined the evolution of ART of individual micro-sized anatase TiO₂ single crystals. The crystal phases of these anatase microparticles were spatially monitored using a Raman microscope after different annealing times and were correlated with the morphological changes in SEM images. The nucleation location of the rutile phase and the gradual progression of the rutile phase in the ART process were observed on each particle. Our results showed that each anatase microparticle showed different phase and morphological evolution pathways during phase transition but are dominated by the surface nucleation and growth. The kinetics of the ART were examined, and the rate constants were determined. Individual particles with a

co-existing anatase/rutile interface were prepared which serve as a perfect platform to study the synergetic effect of anatase/ rutile in photocatalysis.

Experimental section

Micro-sized anatase ${\rm TiO_2}$ single crystals with a high percentage of (001) facets were synthesized by a hydrothermal route developed by Yang *et al.*^{51,53} In our typical synthesis, ${\rm TiF_4}$ was dissolved in a diluted hydrochloric acid (pH around 2) to form a 5.33 mM solution. Next, 30 ml of the ${\rm TiF_4}$ aqueous solution and 90 μ l of concentrated hydrofluoric acid (50 wt%) were added to a Teflonlined autoclave. The mixture was kept at 180 °C for 18 hours in an oven. After the hydrothermal reaction, the white precipitates were collected, washed with DI water and ethanol three times, and then dried in an oven at 100 °C for 6 hours. The anatase crystals were subsequently redispersed in an ethanol solution and were drop cast on a Si substrate.

The annealing process was carried out in the air in a muffle furnace oven. First, the particles were annealed at 600 °C for 2 hours to remove the surface fluoride. Then particles were heated at different temperatures (1000 °C to 1150 °C) for various time durations (from 4 to 50 hours). Raman and SEM measurements were carried out before annealing and after annealing at various temperatures and various time durations to monitor the morphological and structural changes of the particles. Raman spectra showed no evidence of ART when the anatase microcrystals were annealed up to 1000 °C for 20 hours. Most of the anatase crystals started the ART within one or two hours of annealing at 1100 °C. Therefore, the annealing temperature of 1050 °C was chosen to monitor the ART phase transition process with Raman and SEM. In a typical 1050 °C annealing process, the sample temperature was increased from room temperature to 1050 °C with a rate of 10 °C minute⁻¹ and then kept at 1050 °C for 2 hours. After the annealing, the sample was cooled to room temperature for Raman and SEM measurements. Then it was heated up at a ramping rate of 30 °C minute⁻¹ to 1050 °C and kept at 1050 °C for another 2 hours, noted as a total annealing time of 4 hours and so on.

Raman measurements were conducted using a lab-built Raman microscope, which consisted of a 532 nm laser as the excitation source and a Zaber ASR-E closed-loop microscope stage (Zaber Technologies Inc., Canada) for scanning and focusing control. A focused laser beam with a spot size of $\sim 0.7~\mu m$ was scanned over the samples' surface to obtain the chemical information at a submicron level. The Raman spectra were collected using a Princeton Instruments SCT-320 spectrometer with a 1200 lines per mm grating through a $0.85/60\times$ objective lens. Raman maps were collected with a $0.33~\mu m$ step size and 1 second accumulation time. It must be mentioned that mechanical drift can result in slight skewing in some of the Raman maps. This is common and is similar to other scanning imaging methods. 55

Scanning Electron Microscope (SEM) images were collected with an FEI Focused Ion Beam SEM Microscope (FEI-Versa 3D).

Results and discussions

Fig. 1 presents SEM images and representative Raman spectra from several anatase microcrystals (Fig. 1(a)-(c)) and the transformed particles (Fig. 1(d)-(f)) after annealing at 1100 °C for 18 hours. Before annealing, anatase microcrystals expose a large (001) facet surrounded by the {101} facets (Fig. 1(g) inset). Compared to an elongated bipyramidal shape of natural anatase, these microcrystals are of truncated bipyramid. The area of the top (001) facet of Particle #1 (Fig. 1(a)) is measured as 5.1 μ m \times 5.1 µm. Based on the symmetries of anatase microcrystals (Fig. S1, ESI†), 47,51 the percentage of (001) facets is estimated as 88%. The large (001) facet is a characteristic signature of the isotropic growth along $\langle 100 \rangle$ as well as $\langle 010 \rangle$ axes and surmounting the high surface energy of (001) with F⁻ as a stabilizing agent.51

The Raman spectrum taken from the center of the (001) face exhibits an intense peak at 142 cm⁻¹ (Fig. 1(g)), which is identified as an E_g mode of the anatase vibrational spectrum. ^{56–59} The peaks at 395 and 637 cm^{-1} are identified as B_{1g} and E_{g} modes, respectively. The peak at 517 cm⁻¹ is from the partially overlapped peaks from A_{1g} (513 cm⁻¹) and B_{1g} (519 cm⁻¹) of anatase and the Si B_{1g} peak at 520 cm⁻¹ from the substrate. Raman spectra from the whole Particle #1 are presented in Fig. S2a (ESI†). The peak position of the Raman modes from Particle #1 agrees well with the values reported for anatase crystals with large (001) facets. 26,47,57,60

Annealing Particle #1 at 1100 °C for 18 hours induced significant changes in morphology and Raman spectrum. The most noticeable change is the apparent truncation of the upperleft-hand and lower-right hand corners (Fig. 1(d)), transforming the shape from a perfect square to an irregular hexagon. In addition, the angles at the lower-left hand and upper-right hand corners increase from 90° to an oblique angle of 100°. By comparing the images before and after annealing, the area of the top surface of the particle decreased by about 9%. This value is very close the reported volume contraction ($\sim 8.5\%$) between anatase and rutile calculated from the density of anatase (3.89 g cm⁻³) and rutile (4.25 g cm⁻³). 13,31,44 This indicates that there was little change in the thickness of Particle #1.

The Raman spectrum of the transformed Particle #1 indeed shows the vibrational modes associated with the rutile phase (Fig. 1(h)). The Raman spectra from the whole Particle #1 are

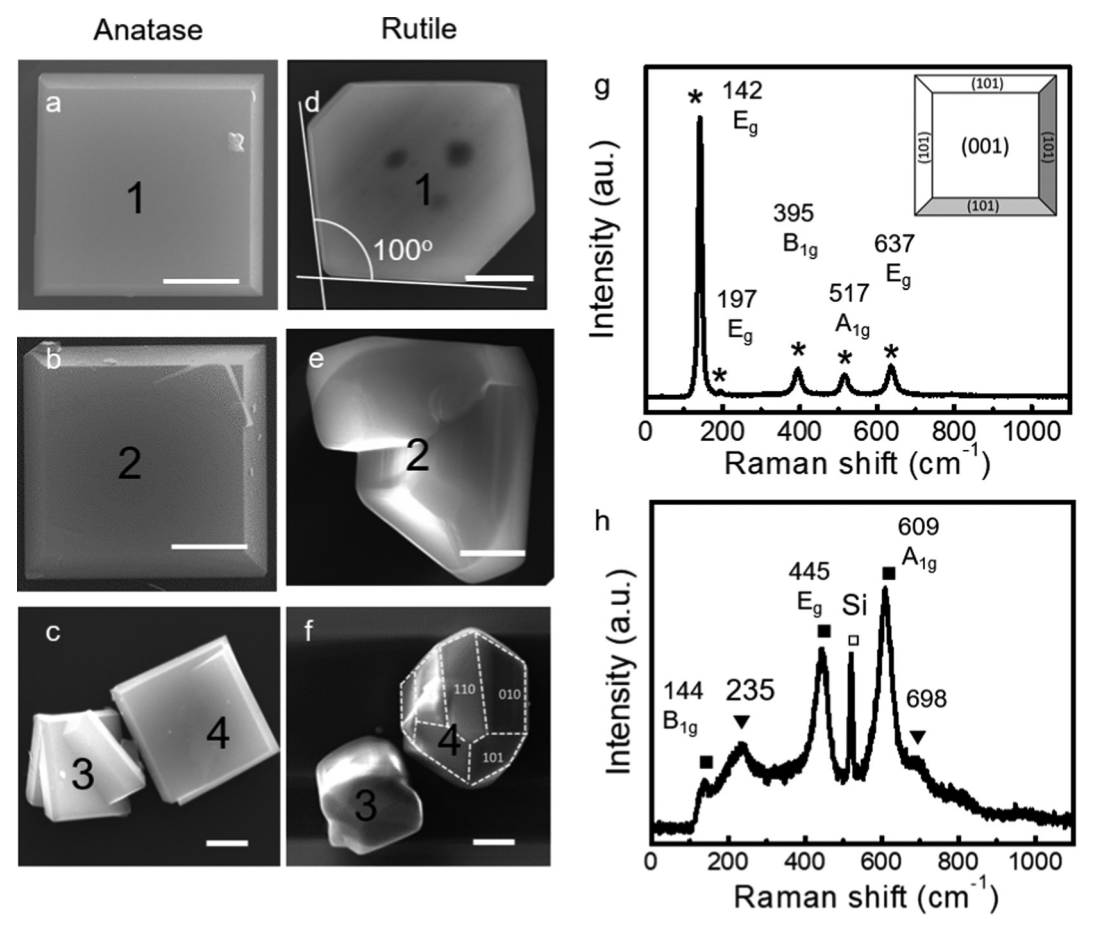


Fig. 1 SEM images and Raman spectra of anatase microcrystals with a large percentage of (001) facets and rutile microcrystals transformed from corresponding anatase microcrystals after 18 hours annealing at 1100 °C. (a) – (c) Top view SEM images of anatase microcrystal Particles #1-#4; (d) – (f) SEM images of rutile crystals after ART from corresponding anatase microcrystals in (a)-(c); (g) Raman spectrum of Particle #1 showing only anatase modes (inset: facets of anatase microcrystals); (h) Raman spectrum of rutile particle transformed from Particle #1 showing only rutile modes. The scale bars in all the SEM images are 2 μm

presented in Fig. S2b (ESI †). The peaks at 144, 445, and 609 cm $^{-1}$ are assigned to the B_{1g}, E_g, and A_{1g} symmetry modes of the rutile phase (D_{4h}), respectively. ^{59,61} The broad peak at 235 cm $^{-1}$ and a shoulder at 698 cm $^{-1}$ are assigned to disorder-induced scattering or second-order effect. ⁶⁰ The peak at 520 cm $^{-1}$ is the Si peak from the substrate as noted before. There is no indication of the anatase phase within the detection level throughout the transformed Particle #1 (Fig. S2b, ESI †).

Fig. 1(b) shows the SEM image of another anatase particle (Particle #2). It is in general of similar shape and size as Particle #1 but has a more substantial defective feature such as a screw dislocation that is noticeable at the upper-right hand corner. After ART, Particle #2 transformed into a twin with the contact plane that is approximately along the square diagonal (Fig. 1(e)). Similarly, Fig. 1(c) presents defective microparticles, Particle #3 and Particle #4. Particle #3 has three intergrown anatase crystals with prominent (001) facets that are interpenetrating approximately perpendicular to each other for one pair. The other pair appears to be contact-twinned with (001) facets slightly tilted from each other. Particle #4 has its own defects: screw dislocations. The annealing transformed Particles #3 and #4 into crystal shapes that are recognizable as a rutile phase (Fig. 1(h)) after comparison with the rutile crystal Wulff reconstruction (Fig. S3, ESI†).62,63 The pronounced boundaries between the assigned low energy facets such as {110}, {010}, and {101} are overlaid on top of the SEM image of the transformed Particle #4. As with Particle #1, Particles #2 through #4 display the Raman peaks associated with the rutile phase only and without any anatase signal throughout the entire particles, showing complete the transformation.

The morphological changes of the particles in Fig. 1 before and after the ART reveal that each particle follows a distinct pathway during the phase transition. In our experiment, Particles #1 through #4 were prepared in the same batch and annealed in the same condition. The complexity of the initial morphological states of the anatase microparticles complicated the ART process, which resulted in rutile microparticles with different morphologies. The ART is also expected to strongly depend on annealing temperature and annealing time as it is a process that involves bond breaking and reforming. We compared particles with similar initial shapes and were annealed at a slightly lower temperature (1075 °C) for 18 hours. As shown in Fig. S4 (ESI†), three particles had similar square top-view SEM images before the annealing (Fig. S4a-c, ESI†). The transformed rutile particles roughly kept their square shapes (Fig. S4d-f, ESI†) after the ART process because of the anatase's topotaxy nature. 64,65 However, the morphology of the particles is different, with one consisting of two grains (Fig. S4e, ESI†) and the other two (Fig. S4d and f, ESI†) having a slightly curved and dipped top surfaces, respectively. Our experiments show that besides the annealing temperatures, the initial morphology, defects, and twinning play important roles in the rutile phase nucleation and growth within the anatase matrix. This observation is consistent with the ART processes reported for natural mineral bulk (millimeter-sized) anatase single crystals in the 1960s.³⁹

To understand the ART process, we monitored the morphology and structural change of the same microparticles at various annealing stages using SEM and Raman spectroscopy. Two anatase microparticles following two distinct pathways are presented below. Particle #5 was annealed at 1050 °C for various total annealing durations from 0 to 50 hours with 2 or 4 hours intervals. A detailed examination of SEM images from Particle #5 is presented in Fig. 2 (see Fig. S5, ESI† for the whole set of SEM images). Before annealing, Particle #5 was measured at 5.5 μ m × 5.5 μ m in a nearly square shape. An (x, y) coordinate system was adopted to define the relative positions addressed in the context.

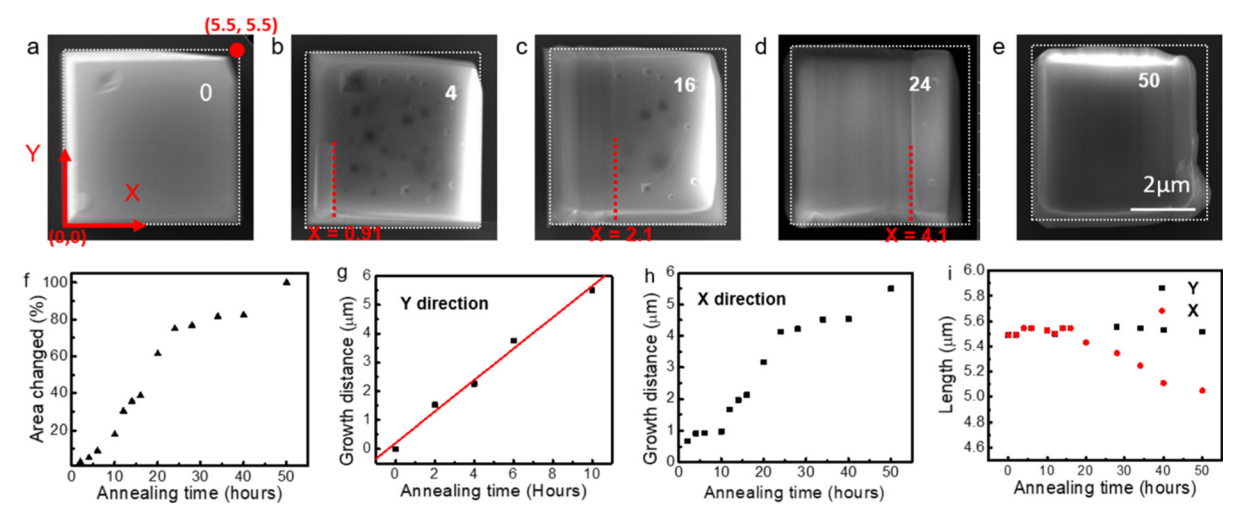


Fig. 2 Representative successive SEM images of an anatase microcrystal (Particle #5) transformed into rutile phase. (a)–(e) SEM images after different total annealing times. The numbers on the images are the annealing times at $1050\,^{\circ}$ C. An (x, y) coordinate system is adopted to define the relative positions that are addressed in the context. The left corner of the particle is defined as (0, 0) and the red dot on the right-top as $(5.5\,\mu\text{m}, 5.5\,\mu\text{m})$. (f) Plot of changed surface area verse annealing time. (g) Plot of growth distance in y-direction y-dire

PCCP Paper

The most obvious defects on the unannealed microparticle (Fig. 2(a)) are a pit near the upper-left corner and an apparent protrusion on the lower-left corner. In addition, the truncation on the upper-right hand corner along with incompletely-developed {101} facets on adjacent sides indicates that there might be other defects on the sides or interior. After 4 hours of annealing (Fig. 2(b)), a markedly striking feature, a lathe, appeared on the lower-left-hand side. The lathe is about 2.3 μm long along the y-direction and 0.91 μm wide in the x-direction.

The continued annealing for a total of 10 hours resulted in the length of the lathe reaching the top end of Particle #5 (Fig. S5f, ESI†). During this period, the width of the lathe increased slightly to 0.95 μ m. The zoom-in images (Fig. S5e and g, ESI†) show that the lathe grows on the surface portion of the particle and the bottom part of the particle stays intact. After 16 hours of annealing, the vertical boundary marked the growth of a new lathe that appeared at $x = 2.1 \mu$ m (Fig. 2(c)). The previously noted pit at the upper-left-hand side completely disappeared, and no trace of the pit defect was noticeable. The vertical boundary continued to move to the right upon further annealing; it reached $x = 4.1 \mu$ m at 24 hours (Fig. 2(d)) and completed the transformation by 50 hours of annealing (Fig. 2(e)).

The fraction of the surface area affected by the lathe formation was plotted as a function of total annealing time (Fig. 2(f)). In the first 10 hours of annealing, the surface area of the lathe-formed region increased to 18%. During this period, the growth can be characterized as quasi-one-dimensional, and the main growth direction was along the *y*-direction with an approximately linear growth rate of 0.55 μ m h⁻¹ (Fig. 2(g)). From 10 hours until 50 hours, the growth direction was along the *x*-direction.

The growth rate is not simply linear; it apparently slows down after 24 hours (Fig. 2(h)). The average growth speed from 10 hours to 24 hours was 0.21 μ m h⁻¹, substantially lower than the growth speed along the *y*-direction. The slowing of the transformation of the surface area happens at around 24 h indicating the accumulated growth stress slowing down the ART process (Fig. S5, ESI†). Overall, Particle #5 exhibits about a 9% reduction in the width along the *x*-direction while the length along the *y*-direction remains about the same (Fig. 2(i)).

Raman maps of the microparticle were collected at each annealing duration to gain chemical and structural insight into the relationship between morphological evolution and the ART process. The SEM image of Particle #5 with 20 hours of annealing at 1050 °C (Fig. 3(a)) was compared to a Raman map created from the spectral intensity integrated from 100 cm⁻¹ to 800 cm⁻¹ (Fig. 3(b)). The Raman map shows the square shape of Particle #5 as in the SEM image but with significant spatial variation in intensity. Two representative Raman spectra (Fig. 3(c), (d), and Fig. S6, ESI†) corresponding to two points (blue and red X marks) in the Raman map show that both phases are present at these locations. The anatase signal is stronger toward the right side of Particle #5 (red) while the rutile signal is stronger toward the left side (blue). The relative concentration ratio of anatase phase and rutile phase can be quantitatively estimated using the integrated area of anatase $\rm B_{1g}$ mode at 395 cm $^{-1}$ and rutile $\rm E_{g}$ mode at 445 cm $^{-1}$ through peak deconvolution (Fig. 3(c) and (d)). The calculated concentration ratio of anatase to rutile is 0.32:0.68 on the left (blue) and 0.63:0.37 on the right (red). The peaks were deconvoluted with Voigt fits as the symmetric Raman bands of mineral crystals are best fitted using either Gaussian-Lorentzian or

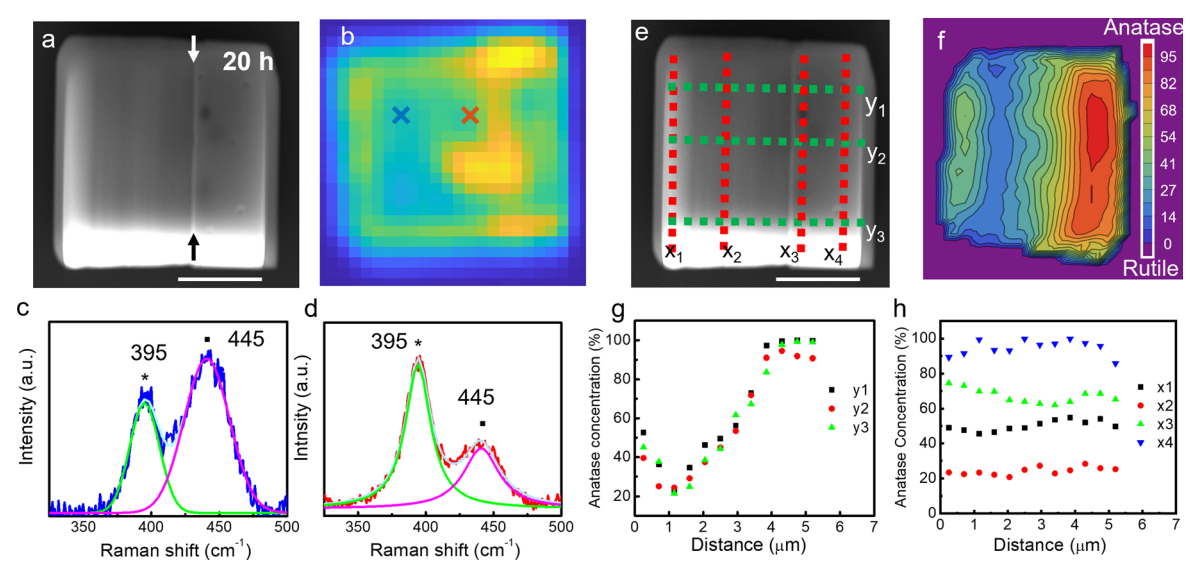


Fig. 3 Phase analysis of a two-phase TiO_2 microparticle, Particle #5 after 20 hours annealing at 1050 °C. Top view SEM image (a) and Raman map (b) from overall intensity between 100 cm⁻¹ to 800 cm⁻¹ of the anatase/rutile-phase microcrystal; deconvoluted Raman spectra (300 cm⁻¹ to 500 cm⁻¹) from the blue cross spot (c) and the red cross spot (d) in panel b. The spectra were deconvoluted into anatase B_{1g} peak and rutile E_g peak using Voigt fits. (e) SEM of the two-phase microcrystal overlaid with the red lines and the green lines representing the position of the Raman spectra for the analysis. (f) Anatase isoconcentration contour map calculated from I_{395}/I_{445} with 6.7% concentration gradient. (g) plot of anatase concentration distribution along y_1 , y_2 , and y_3 ; (h) Plot of anatase concentration distribution along x_1 , x_2 , x_3 , and x_4 . The scale bars in the SEM images are 2 μ m.

PCCP Paper

Voigtian profiles. 66,67 The intensities of anatase B_{1g} and rutile E_g modes were calibrated using bulk commercial single crystals with the same experimental geometry. The detailed calibration procedure is included in ESI† (Fig. S7). The curve fitting results also suggest that at 395 cm⁻¹ (445 cm⁻¹) the spectral intensity is mainly from anatase (rutile) with negligible contribution from rutile (anatase).

A more detailed analysis of the spatial distribution of anatase and rutile concentration for Particle #5 is presented in Fig. 3(e)-(h). The horizontal line scans are shown at three different vertical locations (green dots along y_1 , y_2 , and y_3) in Fig. 3(e). Each line scan consists of 12 horizontal positions where the full Raman spectra were extracted (Fig. S8b-d, ESI†). The anatase concentration falls off from 100% abruptly at x =3.5 µm (Fig. 3(g)), and it approximately coincides with the latheformed borderline in the SEM image as noted in Fig. 3(a). As one moves to the left for each vertical position, there is a clear gradient in the anatase concentration, decreasing to the minimum value of about 25% at $x = 1.1 \mu m$. Interestingly, as we move further to the left, the anatase concentration increases back to a value ranging between 40% to 53%.

Likewise, vertical line scans at 4 different horizontal positions show the variation of the anatase concentration at various places (red dots along x_1 through x_4 in Fig. 3(e)). (Raman spectra were presented in Fig. S8e-h, ESI†). For each horizontal position, the variation of the anatase concentration along the vertical scan is rather small (Fig. 3(h)), compared to that along the horizontal scan (Fig. 3(g)). The anatase concentration at x_1 , x_2 , x_3 , and x_4 is about 50%, 25%, 70%, and close to 100%, respectively. Thus, the gradient of anatase concentration can be

roughly characterized as mainly 1-dimensional, e.g. along the xdirection.

The results discussed above can be summarized into a concentration map of the anatase phase of the entire Particle #5 (Fig. 3(f)). The gradient of anatase concentration along the x-direction between $x = 1.1 \mu m$ and 4.0 μm is clearly seen, irrespective of the vertical locations within the sample. The highest concentration of rutile produced after 20 hours of annealing is observed not at the initial nucleation site (0 µm, 0 µm) but about at $x = +1.1 \mu m$ in a vertical channel with a width of about 0.8 μm .

The ART is a nucleation and growth process. 42,44 From the spatial phase analysis in Fig. 2 and 3, the ART of Particle #5 was dictated by one nucleation location at the corner of the particle surface. The newly-formed rutile lathe was first mainly grown in the y-direction which could be the $[\bar{1}00]$, [100] or [010], $[0\bar{1}0]$ direction on the (001) facet, then gradually spreading out in the orthogonal direction (x-direction) along the surface. The anatase concentration gradient along the x-direction indicates the propagation of the rutile lathe extended into the bulk. The growth front was rectangular which resembles the rectangular growth fronts that were observed on a (001) section of natural bulk anatase single crystals by Shannon et al.39 The almost constant concentration in the y-direction and the linear relationship along the (001) facet in the x-direction show the anisotropic growth behavior. This is expected as the ART kinetics are sensitive to the compressive strain as well as the crystallographic directions. 68 Anatase crystals' {101} facets have lower surface free energy than (001) facets^{32,51} which is the plausible explanation for the higher anatase concentration at the edges of the x_1 .

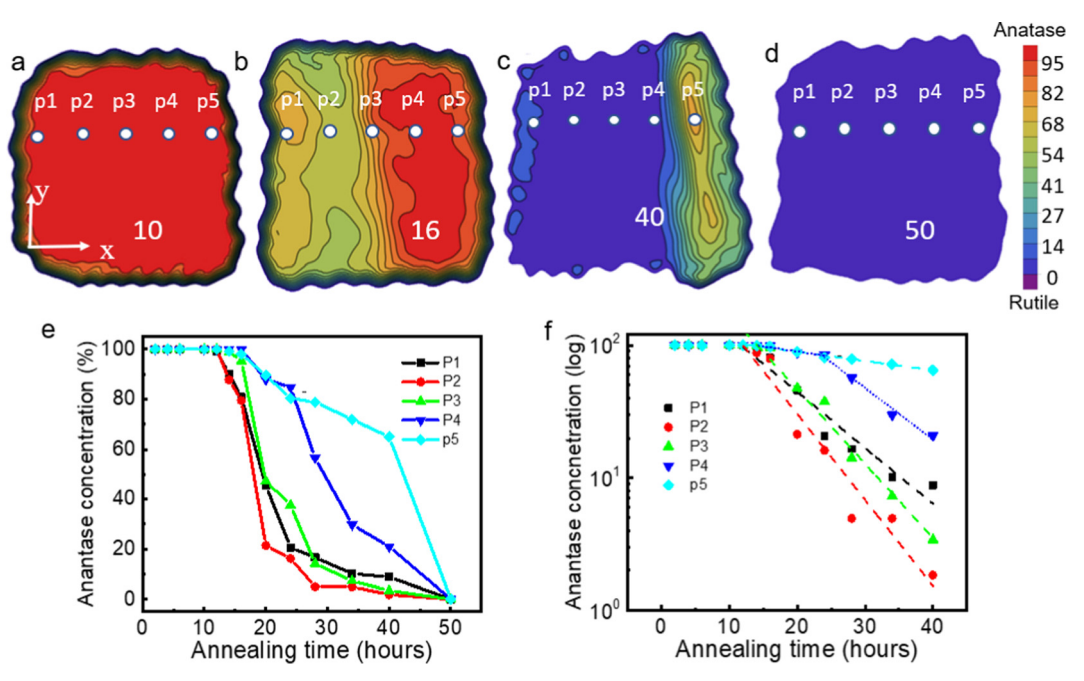


Fig. 4 Temporal evolution of anatase concentration versus annealing time at 1050 °C. (a)-(d) Anatase intensity map with 10, 16, 40 and 50 hours of annealing. (e) Plot of anatase concentration versus annealing time of 5 spots across the particle as shown in (a) to (d). The (x, y) coordinates of the five spots in µm are p1 (0.3, 3.6), p2 (1.3, 3.6), p3 (2.3, 3.6), p4 (4.3, 3.6), and p5 (5.3, 3.6), respectively. (f) Log plot of anatase concentration versus annealing

Paper

Fig. 4 presents the temporal evolution of the distribution of anatase concentration of Particle #5 over the whole ART process. The spectra of the whole particle are presented in Fig. S9 (ESI†). There was no significant formation of rutile in Particle #5 after 10 hours of annealing (Fig. 4(a) and Fig. S9, ESI†). On the other hand, the particle was completely transformed to rutile after 50 hours of annealing with no anatase being observed (Fig. 4(d) and Fig. S9, ESI†). For anatase concentration maps taken after 16 hours (Fig. 4(b)) and 40 hours (Fig. 4(c)) of annealing, the concentration distribution shows a similar trend across the particle as the 20 hours annealing map (Fig. 3(f)). The left part of the particle including the (101) face has a higher rutile concentration compared to the right side. As the annealing time increases, the boundary of high rutile concentration progresses from the left to the right across the (001) face. The left edge, (101) facet part of the particle has a lower rutile concentration compared to the nearby area on the right, although the nucleation started at the left edge.

Anatase concentration from five locations (p1-p5) across the particle was quantitatively analyzed with increasing annealing times at 1050 °C (Fig. 4(e)). To reduce the effect of mechanical drifting during the Raman mapping process, the average of spectra from four pixels close to each of the marked spots was used. The anatase concentrations from the five distinctive positions show different temporal evolution trends. The p1 (black) and p2 (red) show a similar drop in the anatase concentration once the onset of ART occurs. Likewise, the p3 (green) displays a similar drop but after a clear delay of the onset. The p4 (dark blue) and p5 (light blue) show a gradual decrease followed by the similar drop in anatase concentration. The anatase concentration at p3 (green), p4 (dark blue) and at p5 (light blue) clearly indicates that during "the delay" of the onset, there is small but substantial conversion to rutile occurring.

The anatase concentration at the five locations as a function of annealing time is presented in a log plot in Fig. 4(f). The ART follows the first order $\log (1-\alpha) = -kt$ where α is the fraction of transformation completed and k is the rate constant. The slope yields the rate constants. The values of the rate constant are 0.092, 0.14, and 0.14 h⁻¹ at p1, p2 and p3, respectively, and 0.016 h⁻¹ at p5. The rate constant at p5 is about an order of magnitude smaller than those at p1, p2, and p3. This suggests that there are two distinct rate constants. For p4, the data can be fitted with two slopes: 0.016 h⁻¹ during the initial "delay" (12–24 hours) and 0.089 h⁻¹ for 24 through 40 hours of annealing.

The two distinct rate constants can be understood by correlating the ART data with the SEM data. One rate constant is from the surface nucleation and growth, and the other is from the bulk nucleation and growth. From the SEM images (Fig. 2(h)), the surface demarcation line passes through after 6 hours of annealing for p1, approximately between 10 and 12 hours for p2, after 16 hours for p3, 24 hours for p4, and between 40 and 50 hours for p5. The ART with the fast rate $(k_1 = 0.092-0.14 \text{ h}^{-1})$ is indeed observed (Fig. 4(e)) as the lathe boundary passes through or approaches these locations.

With the completed lathe formation, the subsequent ART is dominated by the fast surface transformation as it sweeps through from the left to the right (Fig. 4(b) through Fig. 4(d)) and propagates to the bulk. On the other hand, the slow reaction rate $k_2 = 0.016 \text{ h}^{-1}$ is observed regardless of the location of the surface demarcation line which indicates the bulk nucleation and growth process. For instance, after 20 hours annealing where the boundary line is at $x = 3.2 \mu \text{m}$, the anatase concentration at p5, more than 2 μm away from the vertical line, decreases to 89.5% (Fig. 4(e)).

Various kinetic models have been proposed for ART titania

powder based on ensemble X-ray diffraction studies. Rao et al.

reported that ART followed the first-order law in spectroscopi-

cally pure anatase TiO₂ nanoparticles. 38 This first-order kinetics model assumes random nucleation of particles and rapid surface growth of nucleated particles. 39,44 Despite the age of this study, it is consistent with later studies^{69–71} and the most recent studies. 72 Zhang et al. recently reported that pure TiO2 powder matches the first-order model. 72 Other models have been adopted to describe the ART process for the anatase powders. 39,44,73,74 A model based on a uniform spherical inward growth of spherical particles follows $(1 - \alpha)^{\frac{1}{3}} = kt + c.^{44,73,74}$ When it includes the overlapping of nuclei, the kinetics follows $[\ln(1-\alpha)]^{\frac{1}{3}} = kt + c.^{44}$ An interfacial nucleation and constant growth model was proposed to interpret the ART process of TiO₂ nanocrystalline. 41,43,75 Second-order kinetics is expected in this model because the nucleation involves the interfaces of two contacting anatase grains. To test these models, we have attempted to fit our data with all these models. The secondorder law shows the largest deviation from the data. In our study, since the ART process was monitored on single particles and there are no interfaces of the contacting anatase grains. As expected, the growth kinetics does not follow second-order kinetics. All the other three models (the first-order model, the contracting spherical interface model, and the overlapping nuclei model) fit the experimental data. This is similar to other studies using nanoparticles, in that more than one model could fit the experimental data well. 44,74 In our study, the first-order kinetics fitting shows the best fitting (Fig. 4). Experimentally, Particle #5 exhibited one nucleation spot and grew rectangularly across the particle. The SEM results (Fig. 2) do not support the overlapping of the nuclei model. The contracting spherical interface model suggests the complete coverage of the surface nucleation and the spherical inward growth in the form of a "contracting sphere" from the surface nucleations which is different from the rectangular growth of the particles in our study. The first-order kinetic allows the random nucleation of the particle and is followed by the surface growth of the particle. This kinetic law includes the rate of reaction of both parallelepiped growth and sphere growth. For this reason, firstorder kinetics is the most likely kinetic. The first-order growth kinetics obtained from the Raman measurements in the microsized TiO2 particles combined with the SEM observation suggests that the ART transformation is dominated by surface nucleation and growth (more in the discussion below). This

Paper PCCP

ART process is consistent with the first-order model observed in the nanoparticles. $^{38,69-72}$

Here, the anatase/rutile ratio at a micron level was obtained from an individual anatase microparticle νia combined SEM observation and Raman measurements. The rate constants obtained at 1050 °C in our work are comparable to those obtained from the anatase TiO₂ nanoparticles (\sim 0.04 μ m) at a lower temperature (643 °C) that follow the first-order kinetics. The rate for the micro-sized particles is expected to be slower than that for nanocrystals. Penn and Banfield reported that the reaction rate obtained from larger (millimeter) particle-sized material at a higher temperature (1173 K) is essentially identical to that occurring at a lower temperature (527 K) in nanocrystals.

Fig. 5 presents the SEM and Raman measurements of another anatase particle (Particle #6) which displayed a different ART

pathway. Since Particles #6 and #5 were on the same Si substrate and the physical distance between them was about 60 μ m, the annealing condition of the two particles was identical. Like Particle #5 in Fig. 2, reverse pyramids appeared on the (001) facet after annealing for 6 hours at 1050 °C. Only one nucleation location was observed at the corner of Particle #5, but the nucleation simultaneously occurred at multiple locations on Particle #6 as highlighted with blue circles. Two nucleation sites at the edges and two nucleation sites at the corner of the particles can be identified. There was no detectable rutile signal across the particle at this stage (Fig. 5(b) and (c)).

After 10 hours of annealing (Fig. 5(d)), there were significant morphological changes on the particle's surface at the vicinities of the multiple nucleation sites indicating ART occurred and expanded simultaneously from the edges and corners toward

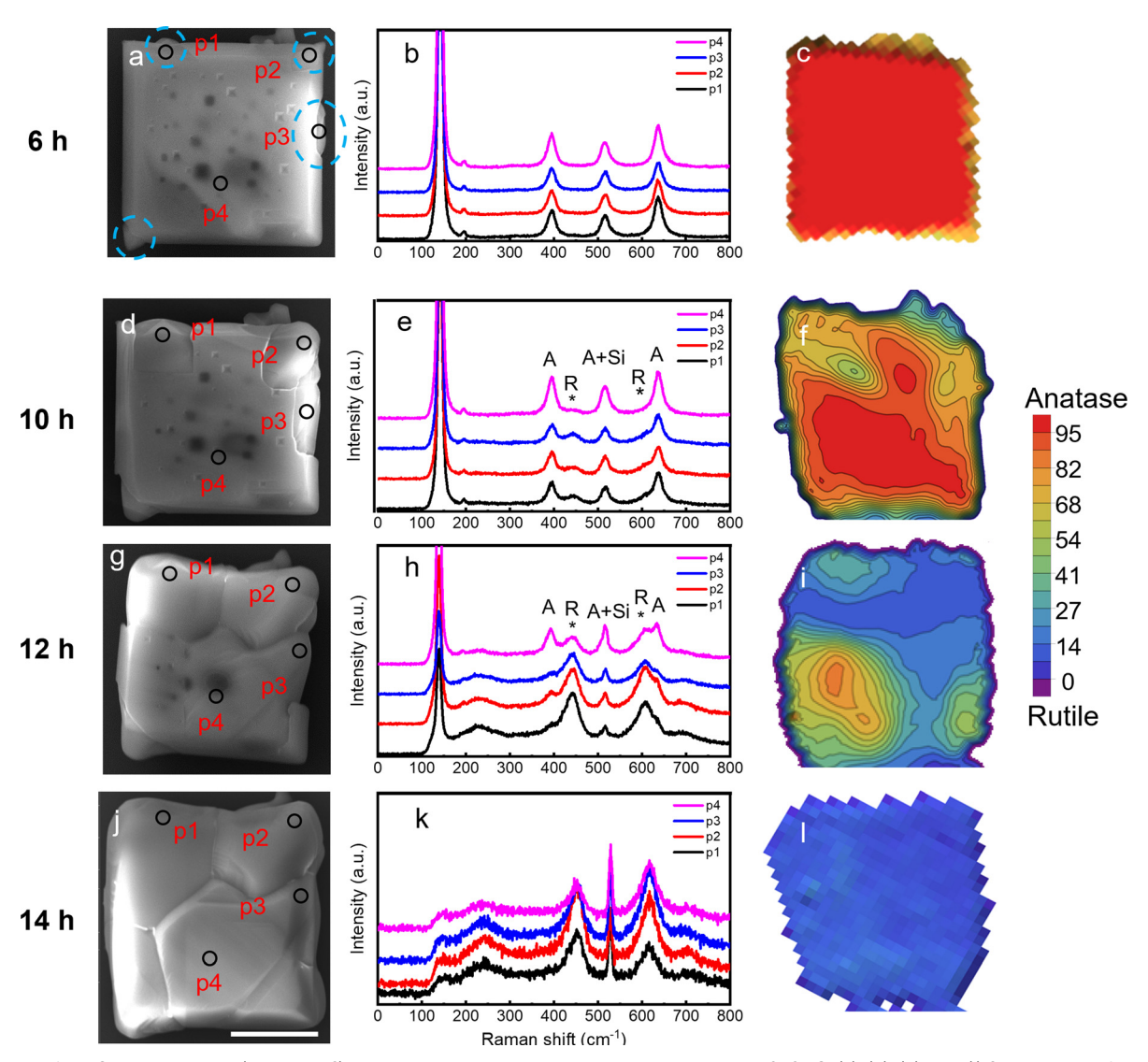


Fig. 5 ART of a TiO_2 microparticle (Particle #6) with multiple nucleation sites when annealed at 1050 °C. (a), (d), (g), and (j) SEM images of Particle #6 after 6, 10, 12, and 14 hours of annealing. Different nucleation sites are highlighted by blue circles in (a). (b), (e), (h), and (k) Raman spectra from Spots p1 to p4 highlighted with black dots in (a), (d), (g), and (j). (c), (f), (i), and (l) Anatase isoconcentration contour map calculated from I_{395}/I_{445} after 6, 10, 12, and 14 hours of annealing. The scale bar is 2 μ m.

PCCP Paper

the bulk of the particles. The morphological changes at individual nucleation locations were different. In the area initiated by the nucleus at p1, the expansion was rectangular on (001) facets. This is similar to the rectangular growth front on Particle #5 and natural anatase bulk single crystals by Shannon et al. 39 The expansion from the other three nuclei was irregular. Although there is slight skewing in the Raman concentration map (Fig. 5(f)) caused by the mechanical drifting during the Raman scanning, the distribution of the anatase phase matches the morphological changes in the SEM image well. The Raman spectra (Fig. 5(e)) from new areas (e.g. spots p1, p2, and p3) show more rutile concentration than those from the unchanged area (spot p4). The rutile E_g mode at 445 cm⁻¹ at spot p4 is weak but distinguishable. As there is no surface nucleation site observed at or near spot p4, the observed rutile concentration would be from the bulk nucleation and crystallization. However, surface transformation dominates the ART of the particle.

After annealing for 12 hours (Fig. 5(g)), the anatase phase continued to retreat towards the center as the rutile phase expanded from the corners and the edges of the particle. The two newly-formed rutile parts reached each other and formed two neighboring grains at the upper portion of the particle. In the spectra from spot p4, the anatase B_{1g} at 395 cm⁻¹ is still stronger than the rutile E_g peak at 445 cm⁻¹. The anatase concentration map (Fig. 5(i)) shows that most of the upper part of the particle transformed into the rutile phase, while the bottom left-hand part of the particle remains mainly anatase. The anatase concentrations at the (101) edge of nucleation site p1 and p2 are higher than the inward vicinities which are consistent with the slow ART transformation speed at the (101) edge as observed in Particle #5. The original anatase particle transformed into five connected rutile grains (Fig. 5(j)) as the ART simultaneously propagated from several nuclei. Since ART involves $\sim 8\%$ shrinkage toward the nucleation sites, the stress from the shrinkage could be why the single crystal cracked into different grains. The Raman spectra across the particle (Fig. 5 and Fig. S10, ESI†) show that the ART of this microcrystal finished after 14 hours of annealing. Among the twelve particles whose ART processes have been monitored individually, the total time it takes for the anatase microcrystals to finish the ART varies from 4 to 50 hours which indicates that the ART process is strongly dependent on the various defects serving as nucleation sites of each individual particle.

Discussion

The Raman and SEM results show that the ART transformation is mainly surface nucleation and growth dominated for the micro-sized anatase particles. For Particle #5, the nucleation occurred at the corner of the particle. Then the surface region adjacent to the nucleation spot was transformed, and this transformed zone expanded through the particle. The growth of the nuclei at the initial stage was mainly on the surface along the crystal edge between (101) and (001) facets with slight

growth into the (001) top facet. No rutile Raman signal was observed until 10 hours of annealing even at the nucleation location (Fig. S11, ESI†). This is likely due to the low crosssection of rutile Raman modes compared to those of the anatase. 23,27,28 Once the rutile phase is detected, the gradient of the rutile phase across the particle supports the propagation of the surface-transformed zone towards the bulk. Otherwise, the surface-transformed portion of the particle would show a uniform rutile concentration from the Raman scattering since the penetration depth ($\sim 0.7 \mu m$) of the 532 nm laser is expected to excite the Raman scattering from both surface and bulk. Particle #6 shows a similar trend of surface crystallization and propagation but with multiple surface nuclei present simultaneously. The contribution of bulk nucleation is noticeable but small which is consistent with what was observed for Particle #5.

The direct comparison of the contribution of the surface nucleation and the bulk nucleation to the ART has not been reported previously. Using UV Raman spectroscopy to probe the surface region and visible Raman spectroscopy to probe both surface and bulk, Zhang et al. reported that for large agglomerated particles (>60 nm), nucleation on the surface, interface, and bulk are all likely to contribute to the ART. 23,27,28 Our results show that while both surface nucleation and bulk nucleation contributes, the surface nucleation dominates the ART for micro-sized anatase particles. This ART process is different from what was suggested for the smaller (<60 nm) nanoparticles^{23,27,28} where the rutile nuclei form in the interior of the particle at interfaces of the contacting anatase grains.

Our experiments show that besides the annealing temperatures, the initial morphology, defects, and twinning play important roles in the rutile phase nucleation and growth within the anatase phase. This observation is consistent with what was reported for natural mineral bulk (millimeter-sized)³⁹ and submicron³⁰ anatase single crystals. Distinctive anatase rutile transformation pathways are attributed to defects, impurities, and the morphology of individual particle, 30,39 as well as the strain between the particles and the substrate.76,77 These nucleation sites in the bulk crystals are on a millimeter-scale. The similarities of the ART processes of bulk, micro-sized, and submicro crystals suggest the possible close correlation of these ART processes with the ART of nanoparticles. Additionally, the two-phased particles provide a perfect platform for studying spatially resolved photoreaction activity at the interface to correlate the synergistic effect of the anatase/rutile phases.

Conclusions

In summary, the ART process of individual anatase microparticles was monitored after various annealing times at the ART temperature using a Raman microscope and SEM. The ART processes of anatase microcrystals with a large percentage (001) facets are distinctive depending on the various rutile nucleation sites. While both surface nucleation and bulk nucleation contribute, the surface nucleation dominates the ART for micro-sized anatase particles. Two types of transition pathways were observed. In one pathway, rutile nucleation

formed at a corner of an anatase crystal and grew along the edge of the microcrystal. The rutile phase then gradually grew orthogonally towards the other side of the microcrystal. The phase concentration calculated from Raman spectra revealed that the ART transition follows the first-order reaction mechanism with two distinct reaction rates, a fast reaction rate from surface nucleation and a slow reaction rate from the bulk nucleation. In the other growth pathway, multiple rutile nucleation sites formed and propagated simultaneously over the particle.

Conflicts of interest

There are no conflicts to declare.

Acknowledgements

Acknowledgment is made to the donors of the American Chemical Society Petroleum Research Fund for partial support of this research. This work was partially supported by the National Science Foundation under Grant CHE-1905043 and the Office of the Vice Provost for Research of Baylor University.

References

- 1 Y. Xia, K. Zhu, Z. Zhang and K. Park, Photo-Stimulated Desorption of Trimethyl Acetic Acid on Cross-Linked (1 \times 2) TiO₂ (110) Probed by Scanning Tunneling Microscopy, *Appl. Surf. Sci.*, 2020, **511**, 145553.
- 2 Z. Zhang, M. Tang, Z. Wang, Z. Ke, Y. Xia, K. T. Park, I. Lyubinetsky, Z. Dohnalek and Q. Ge, Imaging of Formaldehyde Adsorption and Diffusion on TiO₂(110), *Top. Catal.*, 2015, 58, 103–113.
- 3 M. Liang, X. Li, L. Jiang, P. Ran, H. Wang, X. Chen, C. Xu, M. Tian, S. Wang, J. Zhang, T. Cui and L. Qu, Femtosecond Laser Mediated Fabrication of micro/nanostructured TiO_{2-x} Photoelectrodes: Hierarchical Nanotubes Array with Oxygen Vacancies and their Photocatalysis Properties, *Appl. Catal.*, *B*, 2020, 277, 119231.
- 4 M. Chandra and D. Pradhan, Engineering the Morphology and Crystal Phase of 3 D Hierarchical TiO₂ with Excellent Photochemical and Photoelectrochemical Solar Water Splitting, *ChemSusChem*, 2020, **13**, 3005–3016.
- 5 A. Fujishima and K. Honda, Electrochemical Photolysis of Water at a Semiconductor Electrode, *Nature*, 1972, 238, 37–38.
- 6 M. Gratzel, Dye-Sensitized Solar Cells, J. Photochem. Photobiol., C, 2003, 4, 145–153.
- 7 B. Oregan and M. Gratzel, A Low-Cost, High-Efficiency Solar-Cell Based on Dye-Sensitized Colloidal TiO₂ Films, *Nature*, 1991, 353, 737–740.
- 8 L. Kavan, Z. V. Zivcova, M. Zlamalova, S. M. Zakeeruddin and M. Graetzel, Electron-Selective Layers for Dye-Sensitized Solar Cells Based on TiO₂ and SnO₂, *J. Phys. Chem. C*, 2020, **124**, 6512–6521.

- 9 J. Xu, L. Sun, X. Qi, Z. Wang, Q. Fu and C. Pan, A Novel Strategy to Enhance the Multiple Interface Effect using Amorphous Carbon Packaged Hydrogenated TiO₂ for Stable and Effective Microwave Absorption, *J. Mater. Chem. C*, 2019, 7, 6152–6160.
- 10 J. Xu, X. Qi, Y. Sun, Z. Wang, Y. Liu, C. Luo, B. Li, W. Zhong, Q. Fu and C. Pan, Tuning the Electromagnetic Synergistic Effects for Enhanced Microwave Absorption Via Magnetic Nickel Core Encapsulated in Hydrogenated Anatase TiO₂ Shell. ACS Sustainable, *Chem. Eng.*, 2018, 6, 12046–12054.
- 11 J. Augustynski, The Role of the Surface Intermediates in the Photoelectrochemical Behavior of Anatase and Rutile TiO₂, *Electrochim. Acta*, 1993, **38**, 43–46.
- 12 A. Sclafani and J. Herrmann, Comparison of the Photoelectronic and Photocatalytic Activities of various Anatase and Rutile Forms of Titania in Pure Liquid Organic Phases and in Aqueous Solutions, *J. Phys. Chem.*, 1996, 100, 13655–13661.
- 13 D. A. H. Hanaor and C. C. Sorrell, Review of the Anatase to Rutile Phase Transformation, *J. Mater. Sci.*, 2011, 46, 855–874.
- 14 M. Asjad, M. Arshad, N. A. Zafar, M. A. Khan, A. Iqbal, A. Saleem and A. Aldawsari, An Intriguing Case of Morphology Control and Phase Transitions in TiO₂ Nanostructures with Enhanced Photocatalytic Activity, *Mater. Chem. Phys.*, 2021, 265, 124416.
- 15 K. A. Jacob, P. M. Peter, P. E. Jose, C. J. Balakrishnan and V. J. Thomas, A Simple Method for the Synthesis of Anatase– Rutile Mixed Phase TiO₂ using a Convenient Precursor and Higher Visible-Light Photocatalytic Activity of Co–doped TiO₂, Mater. Today: Proc., 2022, 49, 1408–1417.
- 16 X. Wang and C. Li, Roles of Phase Junction in Photocatalysis and Photoelectrocatalysis, *J. Phys. Chem. C*, 2018, 122, 21083–21096.
- 17 D. Jiang, S. Zhang and H. Zhao, Photocatalytic Degradation Characteristics of Different Organic Compounds at TiO₂ Nanoporous Film Electrodes with Mixed anatase/rutile Phases, *Environ. Sci. Technol.*, 2007, 41, 303–308.
- 18 T. Kawahara, T. Ozawa, M. Iwasaki, H. Tada and S. Ito, Photocatalytic Activity of Rutile-Anatase Coupled TiO₂ Particles Prepared by a Dissolution-Reprecipitation Method, J. Colloid Interface Sci., 2003, 267, 377–381.
- 19 Y. M. Sung, J. K. Lee and W. S. Chae, Controlled Crystallization of Nanoporous and core/shell Structure Titania Photocatalyst Particles, Cryst. Growth Des., 2006, 6, 805–808.
- 20 M. C. Yan, F. Chen, J. L. Zhang and M. Anpo, Preparation of Controllable Crystalline Titania and Study on the Photocatalytic Properties, *J. Phys. Chem. B*, 2005, **109**, 8673–8678.
- 21 H. Yao, W. Fu, L. Liu, X. Li, D. Ding, P. Su, S. Feng and H. Yang, Hierarchical Photoanode of Rutile TiO₂ Nanorods Coupled with Anatase TiO₂ Nanosheets Array for Photoelectrochemical Application, *J. Alloys Compd.*, 2016, 680, 206–211.
- 22 Y. Wei, M. V. Tokina, A. V. Benderskii, Z. Zhou, R. Long and O. G. Prezhdo, Quantum Dynamics Origin of High Photocatalytic Activity of Mixed-Phase anatase/rutile TiO₂, *J. Chem. Phys.*, 2020, **153**, 044706.

- 23 B. Anitha and M. A. Khadar, Anatase-Rutile Phase Transformation and Photocatalysis in Peroxide Gel Route Prepared TiO2 Nanocrystals: Role of Defect States, Solid State Sci., 2020, 108, 106392.
- 24 P. Gouma and M. Mills, Anatase-to-Rutile Transformation in Titania Powders, J. Am. Ceram. Soc., 2001, 84, 619-622.
- 25 A. W. Czanderna, C. Rao and J. Honig, The Anatase-Rutile Transition .1. Kinetics of the Transformation of Pure Anatase, Trans. Faraday Soc., 1958, 54, 1069-1073.
- 26 H. Chang and P. Huang, Thermo-Raman Studies on Anatase and Rutile, J. Raman Spectrosc., 1998, 29, 97-102.
- 27 J. Zhang, M. Li, Z. Feng, J. Chen and C. Li, UV Raman Spectroscopic Study on TiO₂. I. Phase Transformation at the Surface and in the Bulk, J. Phys. Chem. B, 2006, 110, 927-935.
- 28 J. Zhang, O. Xu, M. Li, Z. Feng and C. Li, UV Raman Spectroscopic Study on TiO2. II. Effect of Nanoparticle Size on the Outer/Inner Phase Transformations, I. Phys. Chem. C. 2009, 113, 1698-1704.
- 29 W. Lu, B. Bruner, G. Casillas, J. He, M. Jose-Yacaman and P. J. Farmer, - Large Scale Synthesis of V-Shaped Rutile Twinned Nanorods, CrystEngComm, 2012, 14, 3120-3124.
- 30 M. Song, Z. Lu and D. Li, Phase Transformations among TiO₂ Polymorphs, Nanoscale, 2020, 12, 23183-23190.
- 31 J. K. Burdett, T. Hughbanks, G. J. Miller, J. W. Richardson and J. V. Smith, Structural Electronic Relationships in Inorganic Solids - Powder Neutron-Diffraction Studies of the Rutile and Anatase Polymorphs of Titanium-Dioxide at 15 and 295-K, J. Am. Chem. Soc., 1987, 109, 3639-3646.
- 32 U. Diebold, The Surface Science of Titanium Dioxide, Surf. Sci. Rep., 2003, 48, 53-229.
- 33 A. Beltran, L. Gracia and J. Andres, Density Functional Theory Study of the Brookite Surfaces and Phase Transitions between Natural Titania Polymorphs, J. Phys. Chem. B, 2006, 110, 23417-23423.
- 34 K. Hadjiivanov and D. Klissurski, Surface Chemistry of Titania (Anatase) and Titania-Supported Catalysts, Chem. Soc. Rev., 1996, 25, 61-69.
- 35 J. Muscat, V. Swamy and N. Harrison, First-Principles Calculations of the Phase Stability of TiO2, Phys. Rev. B: Condens. Matter Mater. Phys., 2002, 65, 224112.
- 36 M. Batzill, E. Morales and U. Diebold, Influence of Nitrogen Doping on the Defect Formation and Surface Properties of TiO₂ Rutile and Anatase, Phys. Rev. Lett., 2006, 96, 026103.
- 37 A. R. Zanatta, A Fast-Reliable Methodology to Estimate the Concentration of Rutile Or Anatase Phases of TiO2, AIP Adv., 2017, 7, 075201.
- 38 C. N. R. Rao, Kinetics and Thermodynamics of the Crystal Structure Transformation of Spectroscopically Pure Anatase to Rutile, Can. J. Chem., 1961, 39, 498-500.
- 39 R. D. Shannon, In (PhD Thesis) Kinetics and Mechanism of the Anatase-Rutile Transformation, Lawrence Berkeley National Laboratory, LBNL Report#: UCRL-11001, 1964, https://escholarship.org/uc/item/1gs3n995.
- 40 A. A. Gribb and J. F. Banfield, Particle Size Effects on Transformation Kinetics and Phase Stability in Nanocrystalline TiO₂, Am. Mineral., 1997, 82, 717-728.

- 41 H. Zhang and J. F. Banfield, New Kinetic Model for the Nanocrystalline Anatase-to-Rutile Transformation Revealing Rate Dependence on Number of Particles, Am. Mineral., 1999, 84, 528-535.
- 42 R. Penn and J. Banfield, Formation of Rutile Nuclei at Anatase {112 }Twin Interfaces and the Phase Transformation Mechanism in Nanocrystalline Titania, Am. Mineral., 1999, 84, 871-876.
- 43 R. Penn and J. Banfield, Morphology Development and Crystal Growth in Nanocrystalline Aggregates Under Hydrothermal Conditions: Insights from Titania, Geochim. Cosmochim. Acta, 1999, 63, 1549-1557.
- 44 R. D. Shannon and J. A. Pask, Kinetics of the Anatase-Rutile Transformation, J. Am. Ceram. Soc., 1965, 48, 391-398.
- 45 I. M. Clegg, N. J. Everall, B. King, H. Melvin and C. Norton, On-Line Analysis using Raman Spectroscopy for Process Control during the Manufacture of Titanium Dioxide, Appl. Spectrosc., 2001, 55, 1138-1150.
- 46 V. H. Castrejón Sánchez, E. Camps and M. Camacho López, Ouantification of Phase Content in TiO2 Thin Films by Raman Spectroscopy, Superficies Vacio, 2014, 27, 88-92.
- 47 G. Zeng, K. Li, H. Yang and Y. Zhang, Micro-Raman Mapping on an Anatase TiO2 Single Crystal with a Large Percentage of Reactive (001) Facets, Vib. Spectrosc., 2013, 68, 279-284.
- 48 G. Wille, U. Schmidt and O. Hollricher RISE: Correlative Confocal Raman and Scanning Electron Microscopy, Confocal Raman Microscopy, 2nd edn, 2018, vol. 66, pp. 559–580.
- 49 C. R. Das, H. C. Hsu, S. Dhara, A. K. Bhaduri, B. Raj, L. C. Chen, K. H. Chen, S. K. Albert, A. Ray and Y. Tzeng, A Complete Raman Mapping of Phase Transitions in Si Under Indentation, J. Raman Spectrosc., 2010, 41, 334-339.
- 50 R. Penn and J. Banfield, Imperfect Oriented Attachment: Dislocation Generation in Defect-Free Nanocrystals, Science, 1998, 281, 969-971.
- 51 H. G. Yang, C. H. Sun, S. Z. Qiao, J. Zou, G. Liu, S. C. Smith, H. M. Cheng and G. Q. Lu, Anatase TiO₂ Single Crystals with a Large Percentage of Reactive Facets, Nature, 2008, 453, 638-641.
- 52 H. G. Yang, G. Liu, S. Z. Qiao, C. H. Sun, Y. G. Jin, S. C. Smith, J. Zou, H. M. Cheng and G. Q. Lu, Solvothermal Synthesis and Photoreactivity of Anatase TiO2 Nanosheets with Dominant {001} Facets, J. Am. Chem. Soc., 2009, 131, 4078-4083.
- 53 J. Pan, G. Liu, G. Q. Lu and H. Cheng, On the True Photoreactivity Order of {001}, {010}, and {101} Facets of Anatase TiO₂ Crystals, Angew. Chem., Int. Ed., 2011, 50, 2133-2137.
- 54 S. Yang, B. X. Yang, L. Wu, Y. H. Li, P. Liu, H. Zhao, Y. Y. Yu, X. Q. Gong and H. G. Yang, Titania Single Crystals with a Curved Surface, Nat. Commun., 2014, 5, 5355.
- 55 F. Foucher, G. Guimbretière, N. Bost and F. Westall, Petrographical and Mineralogical Applications of Raman Mapping, in Raman Spectroscopy and Applications, ed. M. Khan, IntechOpen, Rijeka, 2017.
- 56 G. A. Tompsett, G. A. Bowmaker, R. P. Cooney, J. B. Metson, K. A. Roders and J. M. Seakins, The Raman-Spectrum of

- Brookite, TiO_2 (*Pbca*, Z = 8), *J. Raman Spectrosc.*, 1995, 26, 57–62.
- 57 T. Ohsaka, F. Izumi and Y. Fujiki, Raman Spectrum of Anatase, TiO₂, *J. Raman Spectrosc.*, 1978, 7, 321–324.
- 58 M. C. Ceballos-Chuc, C. M. Ramos-Castillo, J. J. Alvarado-Gil, G. Oskam and G. Rodriguez-Gattorno, Influence of Brookite Impurities on the Raman Spectrum of TiO₂ Anatase Nanocrystals, *J. Phys. Chem. C*, 2018, 122, 19921–19930.
- 59 W. G. Fateley, F. R. Dollish, N. T. McDevitt and F. F. Bentley, Infrared and Raman Selection Rules for Molecular and Lattice Vibrations: The Correlation Method, Wiley-Interscience, New York, 1972.
- 60 U. Balachandran and N. G. Eror, Raman-Spectra of Titanium-Dioxide, *J. Solid State Chem.*, 1982, 42, 276–282.
- 61 S. P. S. Porto, P. A. Fleury and T. C. Damen, Raman Spectra of TiO₂, MgF₂, ZnF₂, FeF₂, and MnF₂, *Phys. Rev.*, 1967, **154**, 522–526.
- 62 M. Ramamoorthy, D. Vanderbilt and R. D. King-Smith, First-Principles Calculations of the Energetics of Stoichiometric TiO₂ Surfaces, *Phys. Rev. B: Condens. Matter Mater. Phys.*, 1994, 49, 16721–16727.
- 63 M. Barbosa, G. Fabris, M. Ferrer, D. H. de Azevedo and J. Sambrano, Computational Simulations of Morphological Transformations by Surface Structures: The Case of Rutile TiO₂ Phase, *Mater. Res.*, 2017, 20, 920–925.
- 64 R. D. Shannon and J. A. Pask, Topotaxy in the Anatase–Rutile Transformation, *Am. Mineral.*, 1964, **49**, 1707–1717.
- 65 P. Y. Simons and F. Dachille, Possible Topotaxy in the TiO₂ System, Am. Mineral., 1970, 55, 403–415.
- 66 M. S. Bradley, *In Curve Fitting in Raman and IR* Spectroscopy: Basic Theory of Line Shapes and Applications, 2007.
- 67 X. Yuan and R. A. Mayanovic, An Empirical Study on Raman Peak Fitting and its Application to Raman Quantitative Research, *Appl. Spectrosc.*, 2017, 71, 2325–2338.

- 68 S. Zhu, S. Xie and Z. Liu, Nature of Rutile Nuclei in Anataseto-Rutile Phase Transition, *J. Am. Chem. Soc.*, 2015, 137, 11532–11539.
- 69 F. Dachille, P. Simons and R. Roy, Pressure-Temperature Studies of Anatase, Brookite, Rutile and TiO₂-II, *Am. Mineral.*, 1968, 53, 1929–1939.
- 70 S. Vargas, R. Arroyo, E. Haro and R. Rodríguez, Effects of Cationic Dopants on the Phase Transition Temperature of Titania Prepared by the Sol–Gel Method, *J. Mater. Res.*, 1999, 14, 3932–3937.
- 71 S. Liao, Y. Chen, W. Mayo and B. Kear, Transformation-Assisted Consolidation of Bulk Nanocrystalline TiO₂, *J. Am. Ceram. Soc.*, 1999, **11**, 553–557.
- 72 L. Zhang, X. Luo, J. Zhang, Y. Long, X. Xue and B. Xu, Kinetic Study on the Crystal Transformation of Fe-Doped TiO₂ Via in Situ High-Temperature X-Ray Diffraction and Transmission Electron Microscopy, ACS Omega, 2021, 6, 965–975.
- 73 K. Mackenzie, The Calcination of Titania: VI. the Effect of Reaction Atmosphere and Electric Fields on the Anatase– Rutile Transformation, *Trans. J. Br. Ceram. Soc.*, 1975, 74, 121–125.
- 74 E. F. Heald and C. W. Weiss, Kinetics and Mechanism of the anatase/rutile Transformation, as Catalyzed by Ferric Oxide and Reducing Conditions, *Am. Mineral.*, 1972, 57, 10–23.
- 75 J. Wang, A. K. Mishra, Q. Zhao and L. Huang, Size Effect on Thermal Stability of Nanocrystalline Anatase TiO₂, *J. Phys.* D, 2013, 46, 255303.
- 76 K. P. Kumar, K. Keizer and A. J. Burggraaf, Textural Evolution and Phase Transformation in Titania Membranes: Part 1.—Unsupported Membranes, *J. Mater. Chem.*, 1993, 3, 1141–1149.
- 77 K. P. Kumar, K. Keizer, A. J. Burggraaf, T. Okubo and H. Nagamoto, Textural Evolution and Phase Transformation in Titania Membranes: Part 2—Supported Membranes, J. Mater. Chem., 1993, 3, 1151–1159.